Turbulent Eddies in a Compressible Jet in Crossflow Measured using Pulse-Burst Particle Image Velocimetry

SAND2016-0287J

Steven J. Beresh,[a] Justin L. Wagner, John F. Henfling, Russell W. Spillers, and Brian O. M. Pruett

Sandia National Laboratories, Albuquerque, New Mexico 87185, USA

Pulse-burst Particle Image Velocimetry (PIV) has been employed to acquire time-resolved data at 25 kHz of a supersonic jet exhausting into a subsonic compressible crossflow. Data were acquired along the windward boundary of the jet shear layer and used to identify turbulent eddies as they convect downstream in the far-field of the interaction. Eddies were found to have a tendency to occur in closely-spaced counter-rotating pairs and are routinely observed in the PIV movies, but the variable orientation of these pairs makes them difficult to detect statistically. Correlated counter-rotating vortices are more strongly observed to pass by at a larger spacing, both leading and trailing the reference eddy. This indicates the paired nature of the turbulent eddies and the tendency for these pairs to recur at repeatable spacing. Velocity spectra reveal a peak at a frequency consistent with this larger spacing between shear-layer vortices rotating with identical sign. The spatial scale of these vortices appears similar to previous observations of compressible jets in crossflow. Super-sampled velocity spectra to 150 kHz reveal a power-law dependency of -5/3 in the inertial subrange as well as a -1 dependency at lower frequencies attributed to the scales of the dominant shear-layer eddies.

INTRODUCTION

In recent years, time-resolved particle image velocimetry (TR-PIV) has evolved as a means of measuring temporally correlated velocity fields, allowing the acquisition of PIV movies to add a time component to fluid dynamics investigations. Whereas TR-PIV has emerged in a variety of low-speed flows as an adaptation of PIV technology using diode-pumped solid-state kHz-rate lasers and fast CMOS cameras, the requirements of high-speed flows exceed the capabilities of these technologies. Instead, TR-PIV in high-speed flows is best accomplished using a pulse-burst laser, as this is the only light source capable of producing sufficient energy at the necessarily rapid pulse rates, though with the penalty of a very low duty cycle. Simultaneous with the maturation of pulse-burst laser technology, quality high-speed cameras have begun to achieve desirable framing rates without excessive sacrifice of the size of the spatial array. Pulse-burst PIV has a minimal history. Wernet appears to have been the first to achieve pulse-burst PIV,[1] with more recent development offered by Brock et al[2] and Miller et al.[3,4] Pulse-burst PIV had not seen application in a wind tunnel or other testing facility until Beresh et al demonstrated its use in a transonic wind tunnel.[5] A broader view of the usage of pulse-burst laser technology in fluid dynamics instrumentation is given by Thurow et al.[6]

Studies of turbulence in high-speed flows will benefit greatly from pulse-burst PIV's addition of a time-component to

[a] Author to whom correspondence should be addressed. Electronic mail: sjberes@sandia.gov.

full-field velocimetry. One such example would be a supersonic jet exhausting into a subsonic compressible crossflow, studied at considerable length by Beresh et al using conventional PIV.[7-9] In particular, Ref. 8 examined the typical behavior of the turbulent eddies comprising the jet interaction. However, the PIV diagnostic in use at the time could only assess characteristic behavior of the turbulent eddies by conditionally averaging numerous velocity fields at different downstream positions. Pulse-burst PIV, on the other hand, can temporally track each turbulent eddy and therefore directly follow its evolution as it convects downstream. The first demonstration of pulse-burst PIV in a wind tunnel[5] captured the turbulent eddies along the windward shear layer in the far-field of the interaction as the jet mixed with the crossflowing freestream, but were not studied in sufficient depth to elucidate the fluid dynamics of turbulent eddies in this mixing application.

Numerous vortical structures have been identified in jet-in-crossflow interactions and they recently have been ably reviewed by Karagozian[10] and Mahesh[11] with a sketch provided in Fig 1a. Amongst these features are the shear-layer vortices, which are observed instantaneously but have no representation in the mean flowfield other than their influence on mixing. The shear-layer vortices originate from an instability classically attributed to Kelvin-Helmholtz as the jet first begins mixing with the crossflow, then follow the windward boundary of the jet as it turns over and begins to align with the freestream (e.g., Refs. 12, 13). Low-speed experiments indicate that these shear-layer vortices have a prominent role in the formation of the counter-rotating vortex pair (CVP) in the near-field, but once the CVP is established in the far-field, they play a considerably reduced role in the continued production of turbulence and thereby alter the scaling characteristics of the decaying jet.[14-16] The experiments of Megerien et al[17] and Getsinger et al[18] show that the frequency associated with the shear-layer instability is distinct in the near-field but no preferred frequency is found in the far-field, a result supported by the stability analysis of Alves et al.[19]

Although compressible jet-in-crossflow interactions qualitatively maintain the same features as their low-speed counterparts, accumulating evidence suggests that there are differences in the windward shear-layer vortices that affect the downstream growth of the interaction. Several experiments have shown that the large turbulent eddies associated with the windward shear layer are much more persistent downstream for high-speed jets in crossflow and have a more dominant presence,[20-23] an observation supported by several Large-Eddy Simulations (LES).[24-26] This appears to be because the shock structure emanating from the jet nozzle exit is unsteady and deflections of it allow high-speed fluid from the jet to escape into the crossflow with minimal deceleration, altering the formation of the shear-layer vortices in comparison with the dominance of the shear-layer instability at low speeds.[24,26-30] This affects the role of the shear-layer vortices in the far-field of the interaction and appears to give them a prominence comparable to the CVP. Ben-Yakar et al[21] indicate that they appear uniformly spaced in the far-field whereas VanLerberghe et al[27] believe that their periodicity is reduced. Regardless, these

observations suggest that the windward shear-layer vortices play an enhanced role in the far-field behavior of the jet interaction for a compressible flow in comparison to a low-speed flow.

The present work aims to utilize the pulse-burst PIV data that were acquired by Beresh et al[5] to demonstrate the new measurement capabilities, but here analyze them to evaluate the behavior of the shear-layer vortices in the far-field of a compressible jet in crossflow. Whereas the previous article[5] emphasized the measurement capability and demonstrated its use, considerable physical detail may be extracted from the data that lay beyond the scope of the earlier publication. These data offer an opportunity to examine the temporal behavior of these eddies, which has not previously been available for a high-speed flow, and compare it to the better known behavior at low speeds. This can help determine whether the interaction develops differently for a compressible jet.

EXPERIMENTAL APPARATUS

Experiments were conducted in Sandia's Trisonic Wind Tunnel (TWT), which is a blowdown-to-atmosphere facility using air as the test gas. In its solid-wall transonic configuration, the test section is a straightforward rectangular duct of dimensions 305 × 305 mm^2 (12 × 12 inch^2) and any Mach number between 0.5 and about 0.9 may be achieved by adjusting the area of a downstream throat. A nominal Mach 0.8 was tested exclusively for the data used herein with a stagnation pressure of 154 kPa and a fixed stagnation temperature of 321± 2K. The freestream velocity was measured as 285 ± 2 m/s, which is nearer to Mach 0.83 as a result of boundary layer growth in the constant-area test section. The undisturbed boundary layer thickness has been measured as 15.4 ± 0.4 mm at the center of the current field of view and will be mildly thinner at the point of the jet nozzle exit. The test section is enclosed within a pressurized plenum to accommodate ventilated

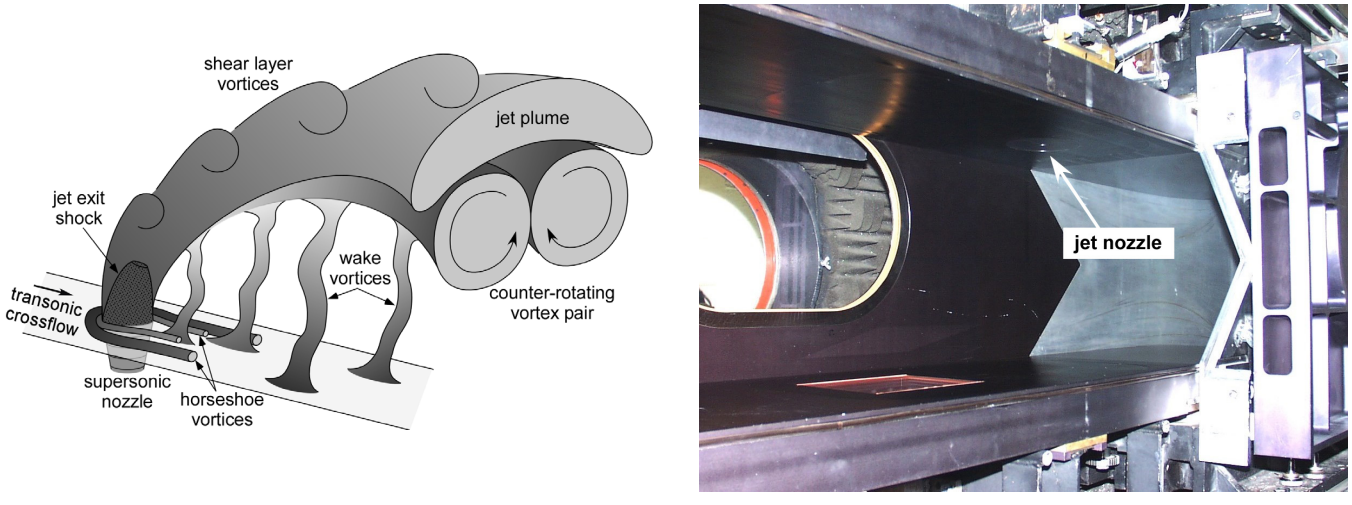

FIG. 1. (a) A sketch of the common features of a jet-in-crossflow interaction. (b) The jet hardware installed into the solid-wall transonic test section of the Trisonic Wind Tunnel. Flow is from right to left.

test sections for other tunnel configurations.

The experiment was configured with a supersonic jet installed on the top wall of the transonic test section upstream of the windows, as seen in Fig. 1b. The upstream location of the jet positioned the imaging region for measurement of the far-field of the jet interaction once it has developed. The laser sheet was introduced through a window in the floor of the test section as well as a matching window in the lower wall of the TWT plenum. It was oriented in the streamwise plane and aligned to the center plane of the test section, which coincides with the center of the jet nozzle exit.

A nitrogen jet exhausted transversely from a conical nozzle with a design Mach number of 3.73, an expansion half-angle of 15 deg, and an exit diameter of 9.53 mm (0.375 inch). The nozzle was fit to a settling chamber designed for a maximum pressure of 14 MPa and instrumented to provide stagnation pressure and temperature measurements. In the present case, the jet was operated at two different conditions; one a pressure of 4.9 MPa to produce a jet-to-freestream dynamic pressure ratio of J=10.2 and the other a pressure of 3.9 MPa for J=8.1. This shifted the position of the jet relative to the field of view, such that J=10.2 data were acquired nearer the core of the jet and J=8.1 farther into the windward mixing layer. The coordinate axes originate at the centerpoint of the nozzle exit plane, with x aligned to the streamwise direction and y positive away from the top wall of the tunnel.

The TWT is seeded by a thermal smoke generator (Corona Vi-Count 5000) that produces a large quantity of particles typically 0.2 - 0.3 μm in diameter from a mineral oil base. Particles are delivered to the TWT's stagnation chamber upstream of the flow conditioning section through a series of pipes and tubes, in which agglomeration of the particles occurs. Previous measurement of the *in-situ* particle response across a shock wave generated by a wedge showed the particle size to be 0.7 - 0.8 μm. Stokes numbers have been estimated as at most 0.05 based on *a posteriori* calculations from the PIV measurements of the instantaneous velocity gradients found in the flow, which is sufficiently small to rapidly attain the local velocity and reduce particle lag errors to a negligible level. The jet itself does not require seeding because all measurements were made in the far field where mixing has entrained and distributed particles throughout the interaction.[7]

In the current work, a quasi-continuous burst-mode laser (QuasiModo-1000, Spectral Energies, LLC) with both diode- and flashlamp-pumped Nd:YAG amplifiers was used to produce a high-energy pulse train at 532 nm. The pulse-burst laser generates up to 10.2 ms duration bursts every 8 seconds with a maximum 532 nm pulse energy of 500 mJ at 5 kHz and 20 mJ pulse energy at its maximum repetition rate of 500 kHz. The laser is capable of producing doublets with variable interpulse spacing at all repetition rates, though in the present work the time between pulses in a doublet was 2.00 μs ± 1 ns. This time was chosen to ensure the largest out-of-plane motions did not exceed 1/6 of the 1.5 mm laser sheet thickness. In this work, 25 kHz doublets were used for PIV measurements with energy per pulse of 175 mJ for a 2.5 ms burst duration. The design of

the pulse-burst laser is based on master oscillator power amplifier architecture and is similar to previously reported pulse-burst-mode lasers.[31-33] Further details about the use of pulse-burst lasers for PIV are discussed by Beresh et al.[5]

Images were acquired using two high-speed CMOS cameras (Photron SA-X2) that have a full framing rate of 12.5 kHz and an array of 1024 × 1024 pixels at this speed. Their windowing function allows the framing rate to be increased by sampling a semi-arbitrary portion of the imaging array. In the present case, each camera operated at 50 kHz with an array of 640 × 384 pixels. The two pulses in a doublet were frame-straddled around the cameras' interframe transfer time, which allowed cross-correlation analysis of pairs of images; thus PIV velocity fields were acquired at 25 kHz. The cameras each were equipped with 200-mm focal length lenses at f-number 5.6.

The two cameras were placed side by side to extend the field of view in the streamwise direction to track the convection of turbulent eddies, yielding a combined field of view of approximately 70 × 21 mm^2 for two-component PIV. Unfortunately, the large size of the camera bodies precluded placing them sufficiently close to one another to image the laser sheet from a normal direction. Therefore, they were canted at an angle of 5 deg such that their individual imaging regions were adjacent and could be combined for vector processing. This angle creates a perspective bias on the velocity vectors due to added sensitivity to the out-of-plane velocity component, but calculations estimate that the maximum induced error is no more than 2%. This was considered to be an acceptable compromise in order to create the desired field of view. A 5-deg angle proved too slight to require Scheimpflug focusing.

Data were processed using LaVision's DaVis v8.2. In each case, image pairs were background-corrected, intensity normalized, and then interrogated with an initial pass using 64 × 64 pixel interrogation windows, followed by two iterations of 24 × 24 pixel interrogation windows. Each step incorporates image deformation with bilinear reconstruction. A 50% overlap in the interrogation windows was used as well. The resulting vector fields were validated based upon signal-to-noise ratio, nearest-neighbor comparisons, and allowable velocity range.

RESULTS AND DISCUSSION

A mean field of the streamwise velocity component acquired from 1500 independent snapshots of a conventional 10-Hz PIV system is shown in Fig. 2 for both the J=8.1 and J=10.2 jets. These data were acquired prior to the pulse-burst PIV and were illuminated by a typical 10-Hz dual-cavity Nd:YAG laser rather than the pulse-burst laser and images were captured using low-speed PIV cameras (LaVision sCMOS). The coordinate origin was centered on the jet nozzle exit and the field of view was established downstream of the nozzle exit and at some distance from the wall to capture the core of the jet and its mixing interface with the freestream. Axes are normalized by the jet nozzle exit diameter, d_j. The location of the decaying jet plume is captured by the streamwise velocity deficit and it can be seen to diminish with downstream distance as the jet

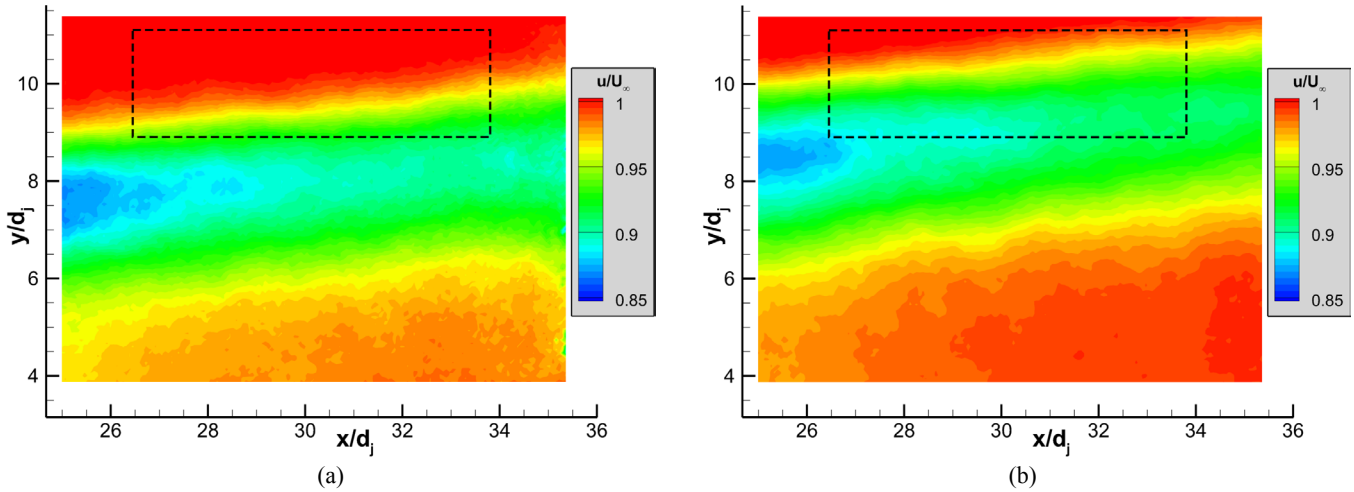

FIG. 2. Mean streamwise velocity component of the jet in crossflow acquired using a conventional 10-Hz PIV system. (a) J=8.1; (b) J=10.2. The dashed rectangular box illustrates the field of view of the pulse-burst PIV.

trajectory slowly moves it outward. The counter-rotating vortex pair will be situated below this trajectory.[7] The dashed rectangular box illustrates the position of the combined field-of-view of the high-speed cameras for the pulse-burst PIV, which is positioned to capture the turbulent eddies to be found at the windward mixing interface. Because the J=10.2 jet penetrates farther into the freestream than does the J=8.1 jet, the same field of view is, in a relative sense, located closer to the jet core in the former case than the latter; this property can be used to study two different locations within the interaction without repositioning the PIV system.

J=8.1 case

A sample velocity field sequence from the J=8.1 data set is shown in Fig. 3, acquired at 25 kHz using cross-correlation analysis. It was extracted from a much longer 2.5 ms burst duration and represents only an eight-snapshot, 280-μs portion of the full burst. The initial time t^*=0 is arbitrary, where nondimensional time $t^* = tU_\infty/d_j$. Velocity fluctuations were found by calculating the mean velocity field over several wind tunnel runs and then subtracting it from each individual velocity field. The plot shows in-plane velocity fluctuations superposed on the derived vorticity field as a color contour and white contour lines denoting the swirl field. In practice, maxima of the swirl field coincide with the vorticity peaks, but provide an unambiguous mark of vortex centers useful for subsequent data analysis. A single pass of light vector smoothing was employed to make features easier to visually track between frames.

Figure 3 shows a counter-rotating pair of eddies entering the field of view on the left edge. As the pair convects downstream, the two eddies can be seen to slowly rotate with respect to one another as they simultaneously drift farther out in the y direction, reflecting the gradual trajectory of the jet. The paired vortices are separated by approximately d_j, the jet exit diameter. A second, weaker pair of counter-rotating vortices can be seen to enter the field of view shortly behind the first

pair, becoming visible at t^*=2.39 at the bottom of the frame. Their orientation is nearly horizontal whereas the first pair entered the field of view nearly vertically oriented. These vortices diffuse with downstream travel and become difficult to detect by t^*=5.98. Yet another pair of counter-rotating eddies enters the field of view at t^*=4.79 and still another at t^*=7.18, each with different rotational alignment. These paired eddies are characteristic of the entire data set, though their stability varies greatly. Some are like the first pair seen initially at t^*=0, remaining sharply defined as they convect and rotate. Others may shear one or both of the eddies into smaller eddies or diffuse vorticity, sometimes leading to a single well-defined vortex seen to remain stable and convect downstream intact. In other cases, out-of-plane motion may remove one or more vortices from the imaging plane. Their relative size also varies from one individual pair to another, with neither the positive nor negative eddy consistently larger than the other. Interestingly, each of the eddies within a pair in Fig. 3 is separated by a reasonably consistent 1 d_j. The distance between pairs is larger, about 2-3 d_j.

A total of 61 bursts were acquired for J=10.2 and 53 bursts for J=8.1, each 2.5 ms in duration. While velocimetry movie sequences such as Fig. 3 can reveal exemplary behavior of the flow, statistical analysis across the entire data set is needed to show the range of behavior of turbulent eddies. As a first step, representative eddy behavior can be found by ensemble averaging the velocity field in a manner similar to that used in Beresh et al,[8] except here the temporal behavior of the eddies may be revealed as well. To accomplish this, a window was created near the upstream edge of the field of view in which the center of the strongest eddy was located and used as an ensemble average condition. Within the range of $26.7 \leq x/d_j \leq 27.5$ and $8.8 \leq y/d_j \leq 10.6$, the position of maximum swirling strength was located to mark the center of the strongest eddy in the window, then the entire flowfield was shifted to the mean position of these eddies over the entire data set. That is, the representative eddy found in the conditional window was repositioned such that their centers coincided at their mean center point. Once co-located, the vector fields were ensemble averaged to produce a representative large-scale eddy. The search procedure used signed swirl, in which the sign of the vorticity at the same location was assigned to the swirling strength to allow positive and negative rotation to be distinguished. A minimum threshold was required to establish the presence of an identifiable vortex.

Since the entire flowfield is repositioned based on the conditional eddy, including subsequent time steps, this allows the typical downstream evolution of the vortex to be recorded. However, the trajectory of each eddy varies somewhat and the ensemble-averaged eddy will appear to quickly dissipate simply due to the varied eddy position. To rectify this, at each subsequent time step, the algorithm once again searches for the swirl peak (though limited to a nearby location) and re-centers the eddy location to the mean location. Therefore, the resulting ensemble-averaged characteristic eddy follows the mean trajectory downstream and displays any decay or distortion entirely due to the eddy's evolution in time and not

variation in position.

Figure 4 shows the ensemble-averaged mean turbulent eddy behavior conditioned on a negative-rotating eddy, displayed on the same scale as the sequence of instantaneous velocity fields in Fig. 3. As the eddy convects downstream, its strength can be seen to gradually diminish, as indicated by both the magnitude of the vorticity field and the length of the velocity vectors. It also is evident that the ensemble-averaged rotation is not uniform, with stronger velocity vectors seen on the upstream side of the eddies as compared to their downstream side. Or viewed differently, velocities have greater magnitudes pointed away from the wall than pointed towards it. At first glance, this may be attributed to superposition of the outward trajectory of the jet, which would enhance vectors aligned to the $+y$ direction and diminish those aligned to $-y$. This cannot be the case, however, as the effects of the jet trajectory would have been removed when the mean velocity field was subtracted to obtain the fluctuating velocity fields.

The ensemble-averaged eddies of Fig. 4 do not reproduce the pairs of eddies commonly seen in the instantaneous data such as that of Fig. 3, in which counter-rotating vortices are often seen separated by about 1 d_j. This suggests that the orientation of these paired vortices is random and evenly distributed, which causes it to average out in Fig. 4 and therefore a paired vortex cannot be found. However, a closer examination of Fig. 4 reveals that a diffuse positive-rotating vortex leads the conditional negative vortex by about 3 d_j and a similar diffuse positive vortex trails it by about 2.5 d_j These spacings appear roughly consistent with the repetition of paired eddies observed in Fig. 3. This suggests that opposite-signed vortices tend to recur at a separation of about 2.5-3 d_j during the mixing of the jet into the crossflow. The repeatability and spacing of these eddies must possess significant variability since the conditional vortex is so diffuse and weak.

Ensemble averages of positive-rotating eddies are given in Fig. 5. Similar to the negative vortex of Fig. 4, the velocity field is nonuniform, though differently than in Fig. 4. Here, vectors are stronger on the downstream side of the vortex, which again is oriented away from the wall. A negatively-rotating vortex is seen more clearly about 2 d_j downstream of the conditional positive vortex, which identifies the strong velocity magnitudes away from the wall as the upwash between two counter-rotating vortices.

The nonuniform ensemble-averaged vortices can be explained by considering the turbulent eddies as pairs. The movie sequence of Fig. 3 clearly shows a tendency for turbulent eddies to occur as counter-rotating pairs separated by about 1 d_j. These pairs then tend to recur every 2.5-3 d_j, also evident in Fig. 3 and suggested by the ensemble averages of Figs. 4 and 5. The contribution from a vortex's counter-rotating complement leads to greater velocity magnitudes in the upwash between them and this creates the nonuniformity seen in Figs. 4 and 5. It is much like the mean velocity field produced by the CVP. The complementary vortex that serves as a counterpart to the representative vortex is faint in the ensemble averages because

its position and strength and perhaps even the probability of its presence varies in time.

To better visualize the presence of paired turbulent eddies, the ensemble-average velocity fields of Figs. 4c and 5c have been recast in Fig. 6 with altered velocity and vorticity scales. Here, all velocity vectors are a uniform length and the vorticity scales have been decreased by an order of magnitude, both changes meant to emphasize the weakly-correlated vortices that were difficult to discern in Figs. 4 and 5. Furthermore, the instantaneous location of the nearest paired vortex is shown by the scatter plot of white data points. Throughout the data set, once the position of the conditional vortex was identified, the nearest vortex of opposite sign was located as well. The same minimum threshold was required as for the conditional vortex. The cloud of data points therefore depicts the location of the counterpart in the pair of turbulent eddies so commonly seen in the movie of Fig. 3 and allows a sense of its orientation at any given moment in time.

Figure 6 indicates that the paired vortex in fact can be seen at a separation consistent with 1 d_j based on the oppositely-signed vorticity now visible, but it is weak in the ensemble averages. On a reduced vorticity scale, it becomes visible but is diffuse due to its variation in position. The cloud of data points representing the instantaneous position of the paired vortex indicates that it can be found at any azimuthal position surrounding the conditional vortex, but there is a weak preference for a position such that the negative vortex leads the positive vortex as they convect downstream. This orientation accelerates fluid away from the wall between the two eddies. The vorticity of the paired eddy is too uncertain to measure the eddy separation, but histograms of the instantaneous vortex positions confirm a most-likely separation of approximately 1 d_j (not shown for brevity). The paired vortex is not evident in the velocity field. Conversely, the uniform-length vectors clearly reveal correlated vortices at a separation of 2-3 d_j. In Fig. 6a, a correlated vortex is seen leading the conditional negative vortex by about 3 d_j, with another correlated vortex following behind by a little more than 2 d_j. Similarly, Fig. 6b shows a leading correlated vortex by 2 d_j and a poorly-converged trailing vortex just entering the field of view nearly 3 d_j behind.

Figure 6 offers evidence that the passage of turbulent eddies correlates in two different ways. First, the paired eddies observed in the movie of Fig. 3 are evident in the 1 d_j separation between the regions of elevated vorticity, most clearly visible in Fig. 6b. This supports the tendency of turbulent eddies to occur in closely-spaced counter-rotating pairs. Secondly, diffuse counter-rotating vortices lead and trail the representative eddy at a distance of 2-3 d_j. These correlated vortices indicate the presence of additional pairs of turbulent eddies preceding and following the reference pair of eddies. Therefore, Fig. 6 visualizes the presence of both the paired nature of the turbulent eddies and the tendency for these pairs to convect through the field of view at repeatable spacing.

Another way to study the pulse-burst PIV data is to perform cross-correlations on the temporal velocity signals across the entire field. This is possible because each velocity vector contains a time history for that point in the flow. This was

accomplished by marking as the reference signal the velocity signal at the center of the ensemble-averaged eddy at t=0 μs and cross-correlating this temporal signal with every other velocity vector in the field of view. The results are shown in Fig. 7 for cross-correlations of the u velocity component and in Fig. 8 for the v component. Correlations on the vorticity have been performed as well but, as should be anticipated, they resemble the ensemble-averaged vorticity fields of Figs. 4 and 5 and hence they are omitted here.

Figure 7 shows that the u component correlates strongly over a region fairly consistent with the size of the characteristic eddy shown in Figs. 4 and 5, possessing an inclination with respect to the coordinate axes. This inclination lies opposite to the jet trajectory. The maximum strength of the correlation decreases as the eddies diffuse and drift from the mean trajectory as they convect downstream. A weak anti-correlation can be seen upstream and downstream of the primary correlation at a distance of 2-3 d_j that appears consistent with the faint counter-rotating vortices detected by the ensemble averages of Figs. 4 and 5. No indication is detected of the paired vortices at a spacing of 1 d_j, which can be attributed to the distributed azimuthal orientation of the pairing as was shown in Fig. 6. Any weak anti-correlation due to the small tendency for the negative eddy to lead the positive would be subsumed by the breadth and strength of the primary correlation.

The cross-correlations on the v component in Fig. 8 tell a similar story but with larger magnitudes. The correlations here are vertically oriented and cover a greater extent than the u component, but still decrease in magnitude as the eddies convect downstream though not as sharply as the loss of u correlation strength in Fig. 7. The most striking difference with Fig. 7 is that Fig. 8 shows the anti-correlations much more distinctly. Both upstream and downstream of the primary correlation, at a distance of 2.5-3 d_j, anti-correlation regions are clearly defined with magnitudes of significant strength, and they maintain their strength even as the primary correlations weaken downstream. Figures 8a and 8f even show a faint positive correlation leading and trailing the anti-correlations by a similar distance. Coupled with the ensemble averages of Figs. 4 and 5, these provide additional evidence that counter-rotating vortices tend to appear in the flow but are not the obvious paired vortices at a distance of 1 d_j seen in Fig. 3. Instead, the spacing between maxima and minima in the cross-correlations indicates the tendency for the paired vortices to recur at a repeatable spacing. Yet the strongest anti-correlation magnitude is only about 0.25, which indicates that these counter-rotating complementary vortices do not occur reliably and may vary somewhat in position, leading to the weakness of the anti-correlations.

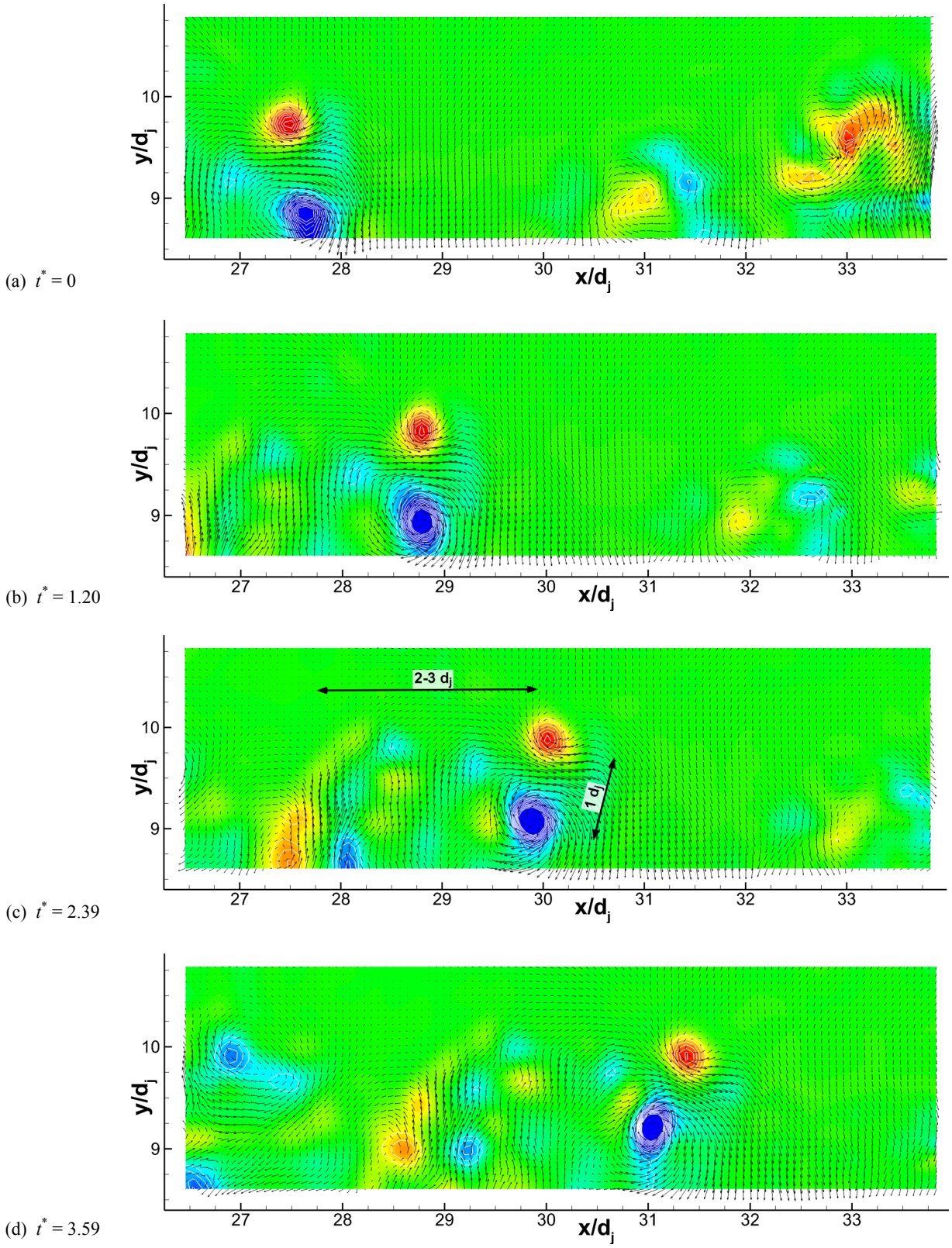

FIG. 3. Sequence of eight velocity fields extracted from a 2.5 ms burst of 58 velocity fields at J=8.1. Vectors show the in-plane velocity fluctuations superposed on a color contour plot of the derived vorticity field and white line contours of the swirl field. Each snapshot is separated by 40 μs. Continued on next page.

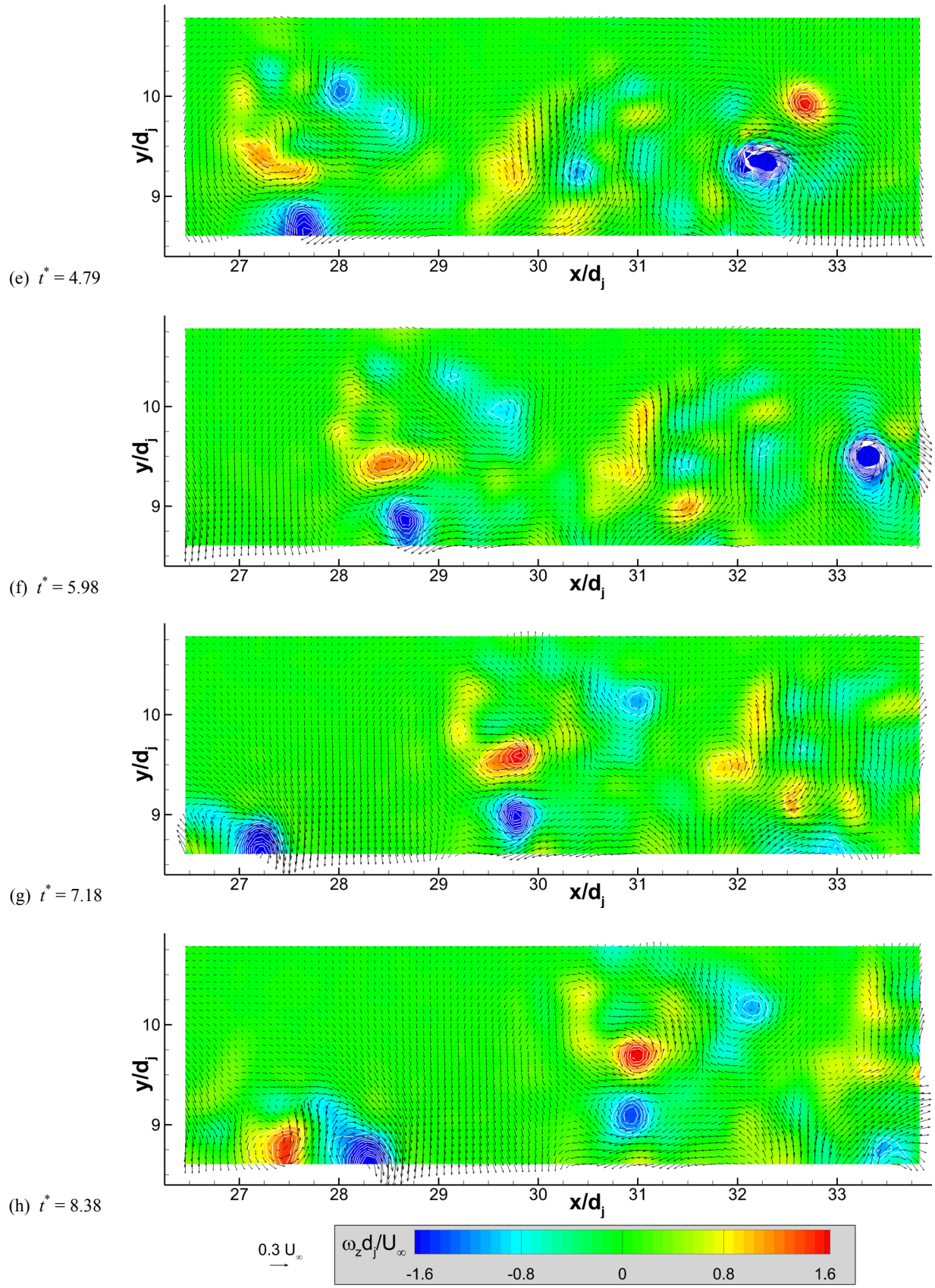

FIG. 3. Continued from previous page.

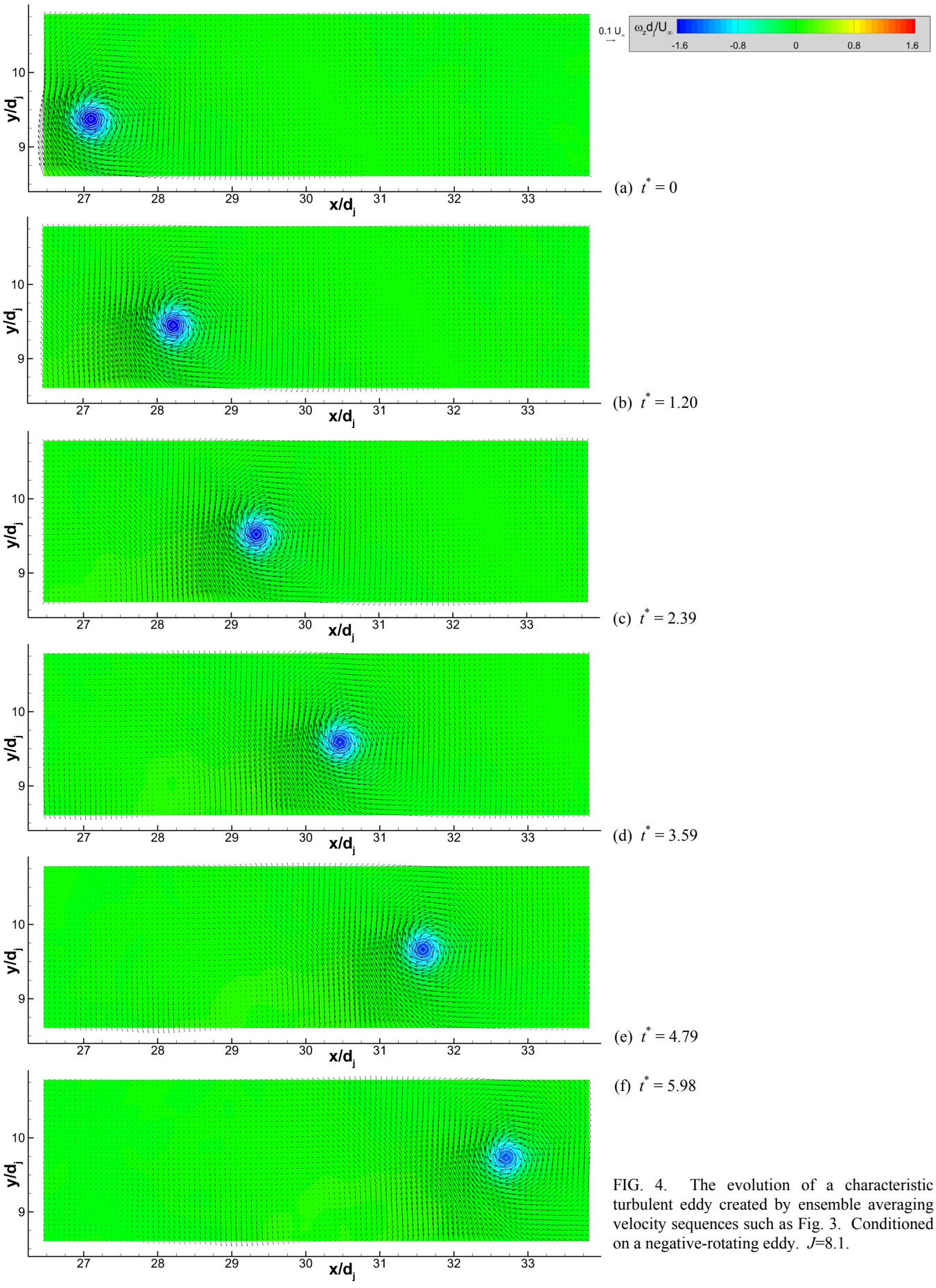

(a) $t^* = 0$

(b) $t^* = 1.20$

(c) $t^* = 2.39$

(d) $t^* = 3.59$

(e) $t^* = 4.79$

(f) $t^* = 5.98$

FIG. 4. The evolution of a characteristic turbulent eddy created by ensemble averaging velocity sequences such as Fig. 3. Conditioned on a negative-rotating eddy. J=8.1.

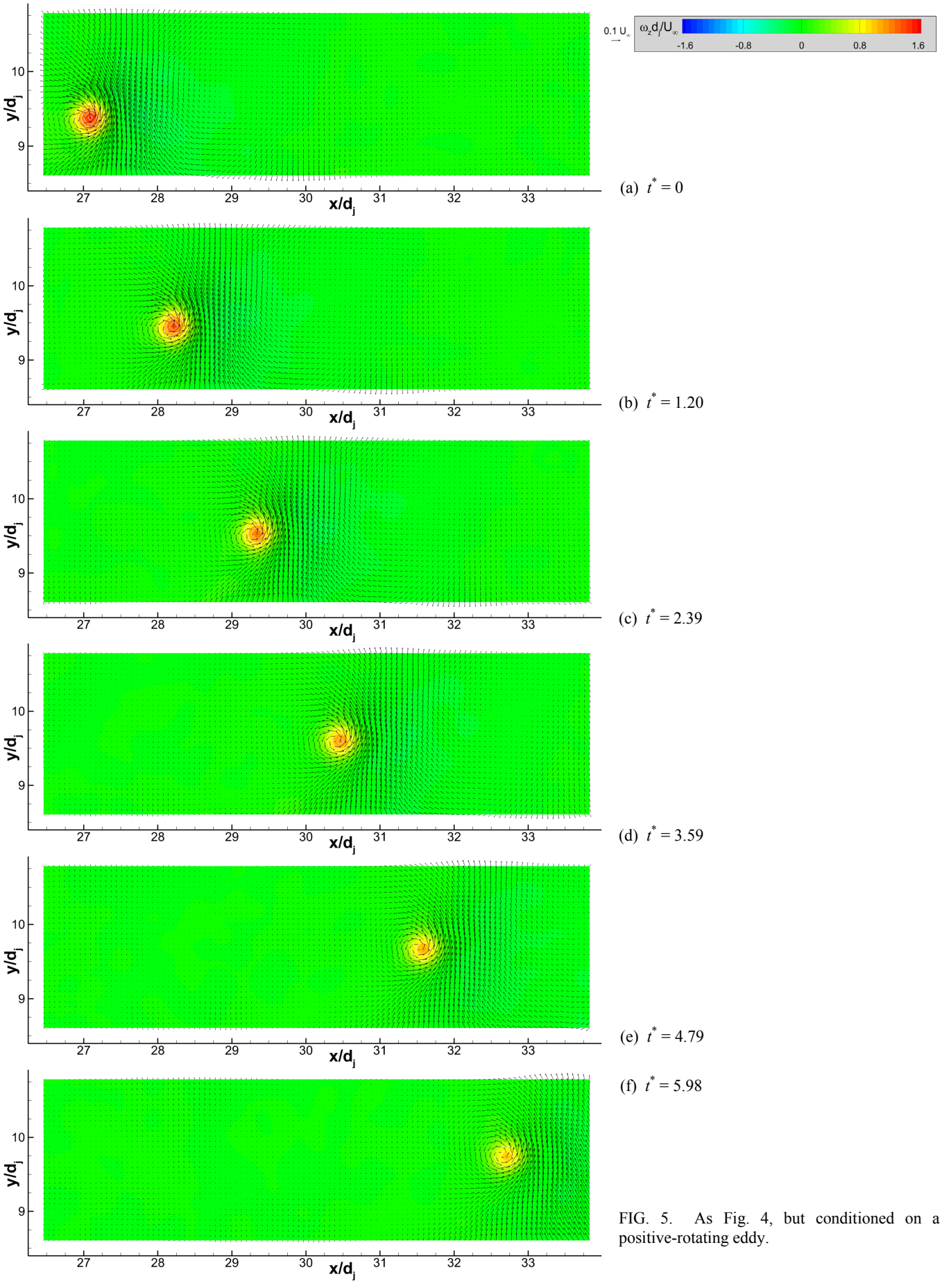

(a) $t^* = 0$

(b) $t^* = 1.20$

(c) $t^* = 2.39$

(d) $t^* = 3.59$

(e) $t^* = 4.79$

(f) $t^* = 5.98$

FIG. 5. As Fig. 4, but conditioned on a positive-rotating eddy.

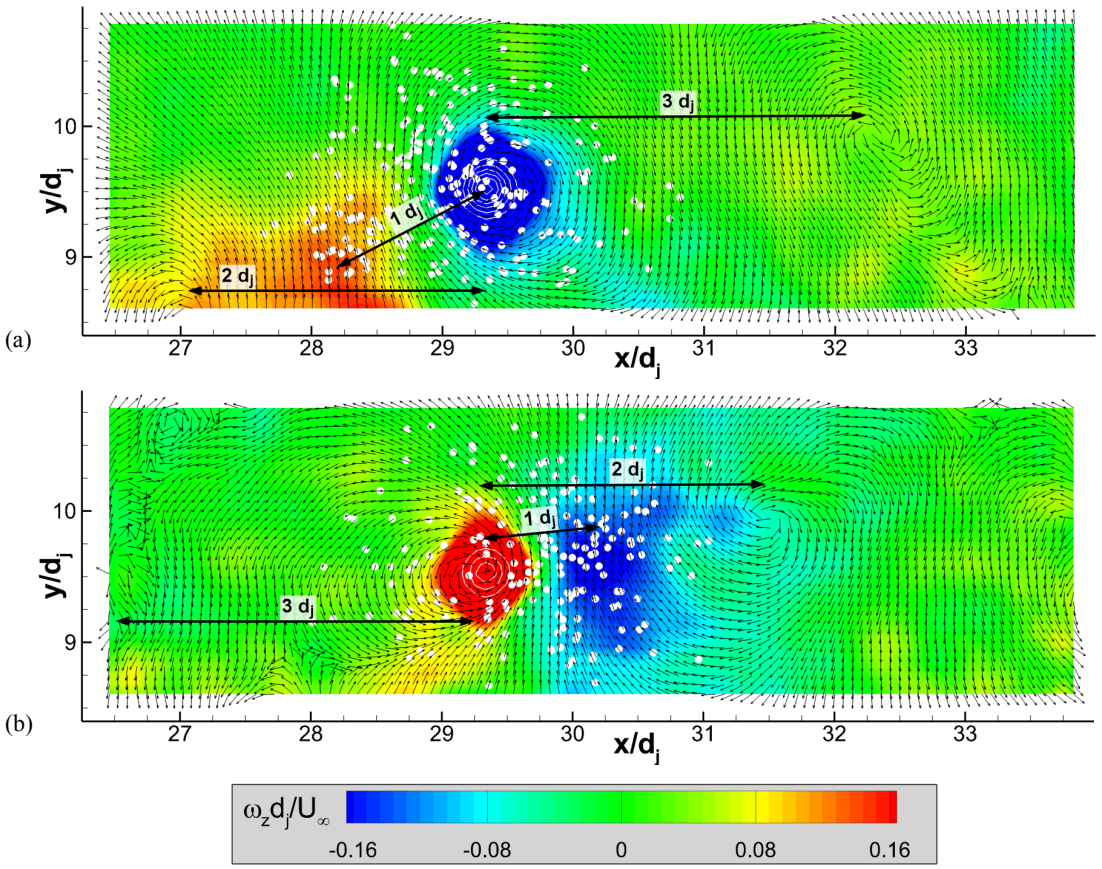

FIG. 6. An alternative visualization of the ensemble-averaged velocity fields of a characteristic turbulent eddy at t^*=2.39, with constant-length velocity vectors and reduced vorticity scale. J=8.1. White data points identify instantaneous locations of the paired vortex. (a) negative rotating eddy; (b) positive rotating eddy.

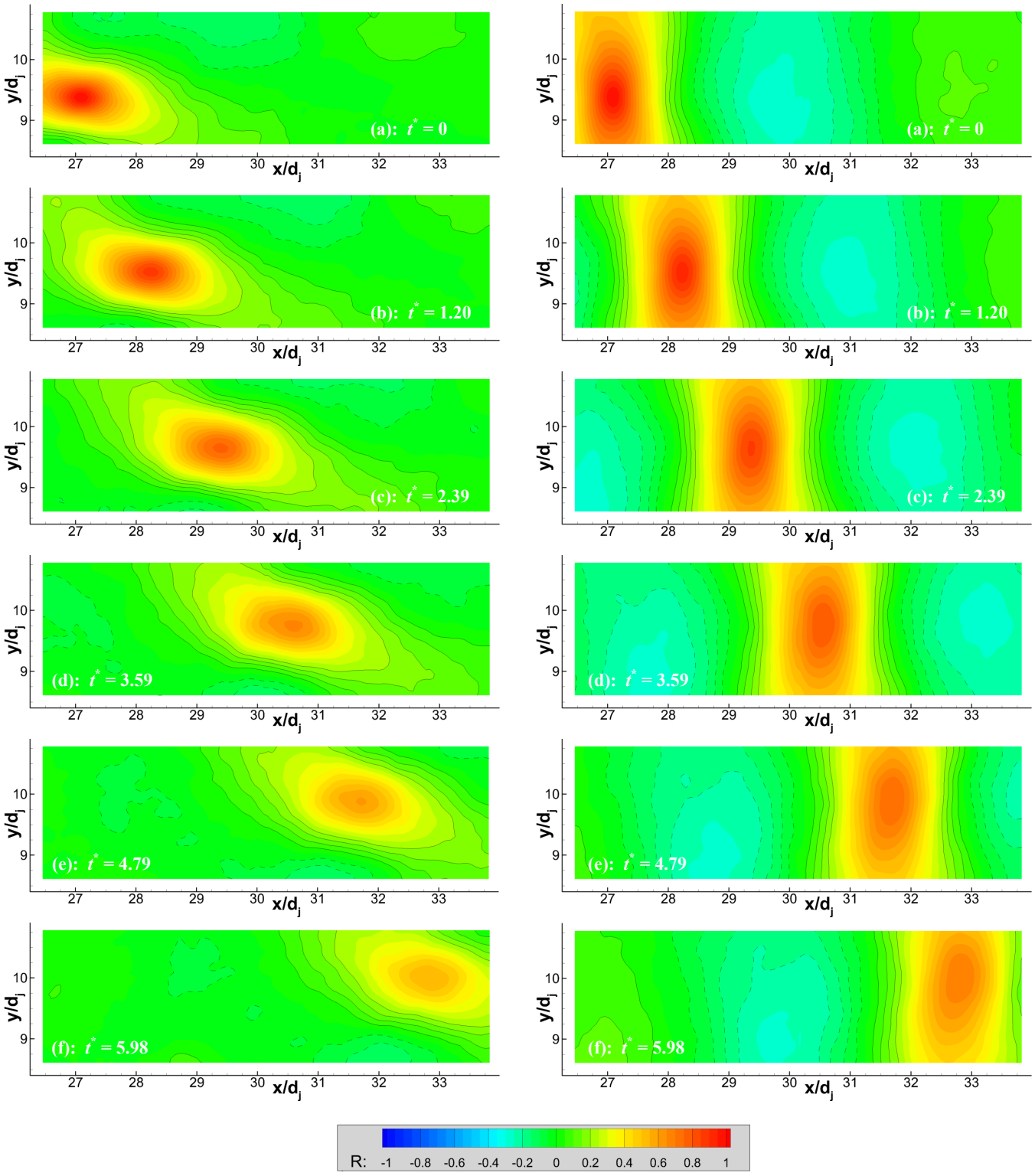

FIG. 7. Sequence of temporal cross-correlations of the streamwise velocity component with reference point at the center of the t^*=0 ensemble-averaged vortex. Line contours emphasize the correlation level at intervals of 0.05 in the range of ±0.2, with dashed lines for anti-correlations. J=8.1.

FIG. 8. As Fig. 7, but for the vertical velocity component.

J=10.2 case

The J=10.2 data tell essentially the same story as the J=8.1 case despite the field-of-view being located closer to the jet core, and hence are supplied here in abbreviated form. A short sequence of velocity fields is shown in Fig. 9, though only four frames are given this time. Many more turbulent eddies are found than at J=8.1, which complicates the visual interpretation of the flowfield. Still, a tendency for paired counter-rotating eddies at a separation of about 1 d_j is illustrated by these vector fields. This is most evident in the strong pair that enters the field of view in Fig. 9a at about y/d_j=10.25 and convects downstream in subsequent frames. Careful scrutiny suggests additional paired vortices, but the greater prevalence of turbulent eddies of both signs makes visual analysis ambiguous.

Conditional averages of the J=10.2 data look identical to those of the J=8.1 data in Figs. 4 and 5, except that the vorticity magnitudes are slightly larger and the characteristic eddies follow a different trajectory. Replotting with a constant velocity scale and reduced vorticity scale as in Fig. 6 also is quite similar, revealing weak counter-rotating vortices leading and trailing the characteristic vortex by 2.5-3 d_j and a smudge of elevated vorticity at about 1 d_j from the characteristic vortex corresponding to the paired turbulent eddies. The consistency of the J=8.1 and J=10.2 ensemble-averaged vortices indicates that the same characteristic behavior of turbulent eddies is found nearer to the jet core despite their greater quantity. The J=10.2 ensemble-average plots are omitted due to their strong resemblance to those already presented at J=8.1.

Cross-correlations also were performed on the J=10.2 data and are given in Figs. 10 and 11 for the u and v components, respectively. Again, the similarity with the J=8.1 data in Figs. 7 and 8 is evident. However, the correlation strength is found to be weaker for J=10.2. As time progresses, the strength of the correlation falls with downstream distance at a faster rate than for J=8.1, and this is true for both the u and v components. Moreover, the anti-correlations are noticeably weaker as well. In the u component they have almost entirely disappeared; in v they are still distinct but the maximum correlation level is mildly diminished in comparison with J=8.1. These reduced correlation levels may be a reflection of increased turbulent activity nearer the core of the jet plume, where the greater quantity of turbulent structures as witnessed in Fig. 9 masks any ordered progression of eddies to a larger extent.

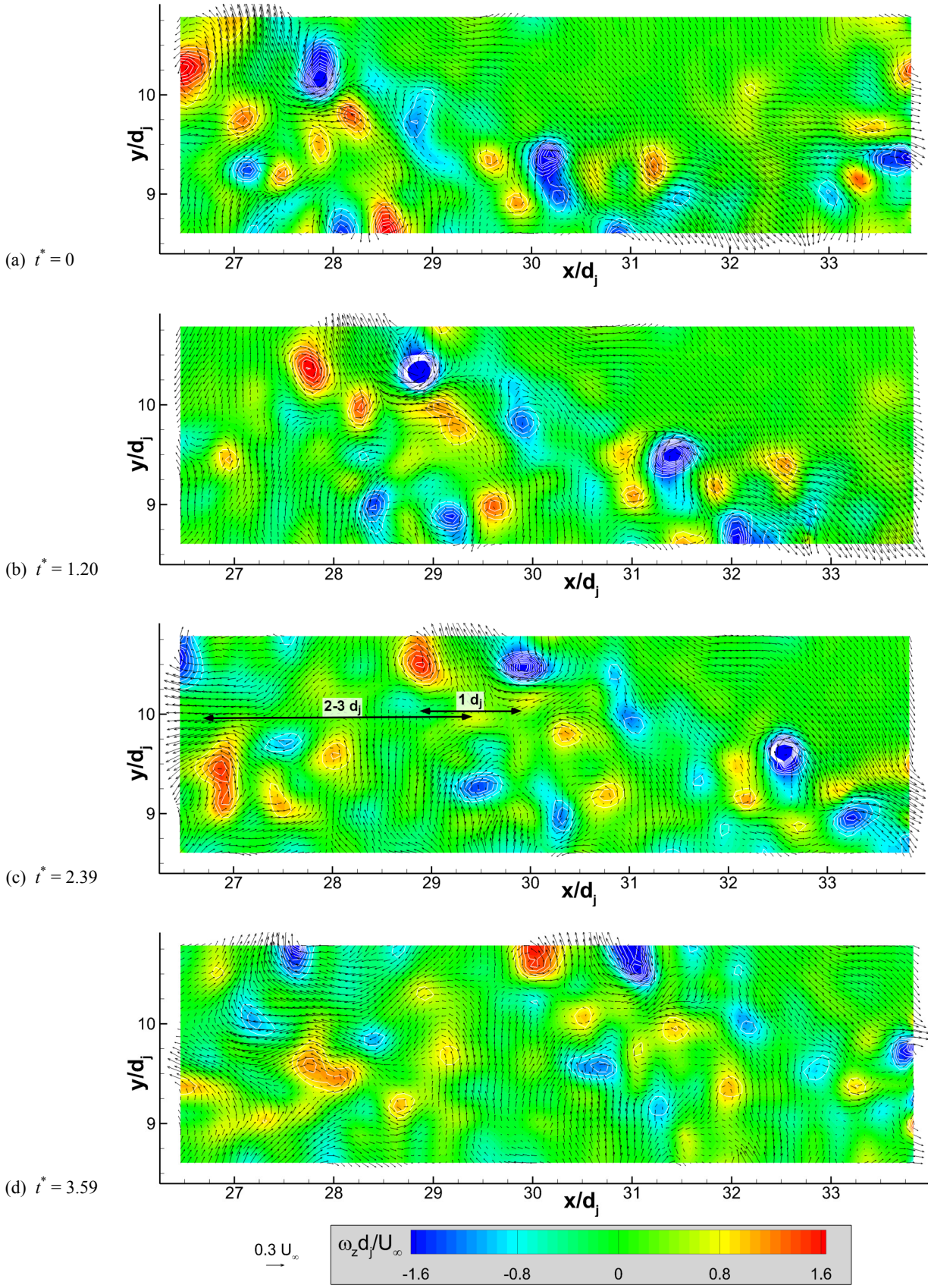

FIG. 9. As Fig. 3 but a sequence of four vector fields at J=10.2.

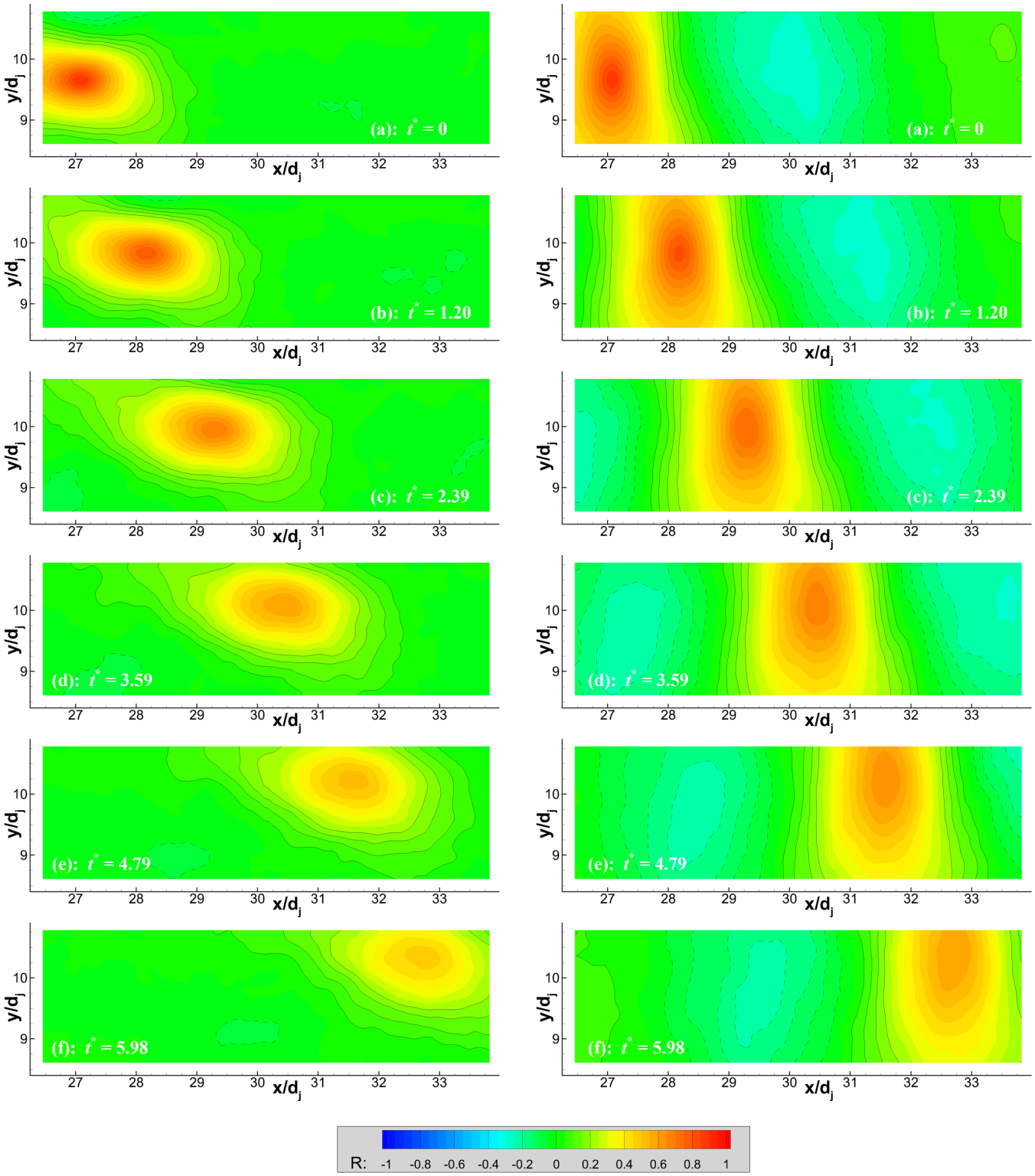

FIG. 10. Cross-correlations of the streamwise velocity component as Fig. 7, but J=10.2.

FIG. 11. As Fig. 10, but for the vertical velocity component.

Power Spectra

The tendency for turbulent eddies to occur in repeatably-spaced counter-rotating pairs suggests that a characteristic frequency ought to be observed in spectra of the velocity fluctuations. One of the most powerful contributions of pulse-burst PIV is the ability to measure velocity frequency spectra across an entire field of view. In the present case, however, the properties of the jet interaction change very little across the present field of view and it suffices to examine the spectra at two points. Figure 12 shows the power spectral density (PSD) at two points, one at the mean location of a turbulent eddy upstream (i.e., its position in Figs. 4a and 5a) and another downstream (Figs. 4f and 5f). These points are different for J=8.1 and 10.2 in their vertical positions, reflecting the differing mean trajectories. Also included are data acquired at twice the acquisition rate, 50 kHz, by double-exposing particle images on a single frame and interrogating images using auto-correlations.[5] This is accomplished at a penalty of poorer spatial resolution and increased uncertainty, but is possible because there are no reverse velocities in the present flow. Spectra were computed using unsmoothed vector fields. Two PSD plots are shown, one for the streamwise component of velocity fluctuations and the other for the vertical component. Frequency axes are given in both absolute and nondimensional forms.

The PSD's of the streamwise component in Fig. 12a show approximately flat spectra prior to the rolloff at higher frequencies, but the vertical component PSD's in Fig. 12b display a distinct peak. The peaks of the power spectra in Fig. 12b reside at about 4 - 5 kHz (Strouhol number about 0.15) with no appreciable difference between the upstream and downstream locations or significant difference as a function of J. Previous studies to examine spectra of jet-in-crossflow velocity fluctuations typically have been low-speed flows intended to measure instability frequencies in the near-field,[12,17,34,35] but some compressible computations show spectra farther downstream of the jet exit for the streamwise component,[36] the spanwise component,[24] and the turbulent kinetic energy,[28] all of which resemble those of Fig. 12a. No known previous study detected a frequency peak as in Fig. 12b, but neither did any of the known studies publish results from the vertical velocity component. The differing appearance of the vertical component may be because it reflects the upwash between paired turbulent eddies as visualized in the present PIV data.

The peak frequency in Fig. 12b roughly corresponds to a distance of 5.9 – 7.4 d_j, assuming a convection velocity equivalent to the freestream velocity. In reality, the convection velocity within the jet plume will be a little slower than this so the corresponding distances will be a little shorter as well. In fact, tracking the characteristic eddies in Figs. 4 and 5 yields a convection velocity of about 0.93-0.95 U_∞, lowering the frequency-based eddy spacing to 5.5 – 6.9 d_j. The separation between vortices of opposite rotation in the ensemble averages of Fig. 6 and the distance between positive and negative correlation peaks in Figs. 8 and 11 were found to be 2.5 – 3 d_j. Therefore a full period – that is, the separation between vortices of identical sign – is about 5 – 6 d_j. This corresponds passably well to the peak frequency observed in the PSD's of

Fig. 12b, suggesting that the tendency towards orderly passage of vortex pairs is identifiable in the frequency content of the flowfield.

The paired turbulent eddies do not resemble the classic Kelvin-Helmholtz instability that generates rollers of a single direction of rotation, but an increasing understanding has emerged in the literature that even in a low-speed flow the instability of the jet-in-crossflow shear layer may differ from that of the free jet.[10,17,37-41] Neither should a frequency corresponding to the Kelvin-Helmholtz instability be anticipated here. Nevertheless, the present measurements offer evidence of a residual preferred frequency well downstream of the initiation of the flowfield and a weak tendency toward ordered turbulent eddies in the shear layer. Some precedent does exist in low-speed flow for the observed vortex pairing. Kelso et al[42] were the first to detect this phenomenon, but their discovery is supported by the studies of Camussi et al[38] and Cambonie and Aider.[43] Collectively, these experiments indicate that one vortex in each pair originates at the windward shear layer and is then joined by a counter-rotating counterpart arising from the leeward shear layer. These appear to begin at a separation distance equivalent to the jet exit diameter and then gradually grow apart with downstream distance. This increasing separation would suggest that, in the present data, they may appear as the vortices paired at a distance of 2.5-3 d_j, not those of 1 d_j separation, particularly considering their stable orientation with respect to the jet trajectory. New et al[44] similarly demonstrated vortex pairing in the shear layer but did not indicate increasing separation downstream. The paired eddies on a 1 d_j scale may be related to ejection of high-speed jet fluid through the unsteady jet shock structure,[24,26-30] which would not have an analogue in low-speed flows.

However, it is not obvious whether the vector fields have detected large-scale vortices within the jet plume that would resemble those found by Ben-Yakar et al[21] or Takahashi et al,[22] which suggested structures roughly two jet diameters in size along the windward mixing layer, or VanLerberghe et al[27] whose structures were approximately half that. Computations by Watanabe et al[25] and Peterson and Candler[26] are consistent with these experimental observations. But the apparent structure size is dependent upon the means of measurement. The aforementioned studies used schlieren and planar laser-induced fluorescence to qualitatively image the jet mixing. Comparisons of the present velocity fields to these imaging methods contain considerable ambiguity. Figures 4 and 5 suggest eddy diameters on the order of 0.5 - 1 d_j, depending on whether the velocity vectors or vorticity field is examined. This is smaller than those found using conventional PIV in the same flowfield;[8] the poorer spatial resolution of the earlier experiment effectively acts as a low-pass filter and may explain the discrepancy. The cross-correlations of Figs. 7, 8, 10, and 11 suggest coherent eddies that are easily 2 d_j in extent and perhaps larger; cross-correlation analysis can be expected to yield a lower-frequency representation of the flowfield than an ensemble-average. In an imprecise sense, the presently detected vortices do bear some similarity to earlier measurements.

However, a more rigorous comparison is not feasible because the present data were collected farther downstream than comparative experiments, and moreover the jet is overexpanded rather than underexpanded, which alters the shock structure at the nozzle exit. Values of J differ as well. An exception is Chai and Mahesh,[29] who computed the present flowfield but have not published analysis suitable to a comparison with the present data. Given the limited range of the experimental conditions and the aforementioned ambiguities, the present data can be said to be consistent with previous observations of compressible jets in crossflow, but an exacting comparison is impractical.

Conversely, considerable additional quantitative information is available from the temporal aspect of the pulse-burst PIV data. The power spectra of Fig. 12 contain useful information at frequencies exceeding that of the peak in Fig. 12a and corresponding to spatial scales smaller than the large-scale vortices discussed to this point. At high frequencies, the correlation noise of the cross-correlated data becomes evident at about 8 kHz and appears to initiate a noise floor, whereas the higher-frequency noise in the auto-correlated data appears at about 15 kHz and continues a trend of diminishing energy as frequency rises. Aliasing may also be present at higher frequencies, artificially raising their magnitudes. It is well-known that the velocity power spectra should obey a power-law dependency of -5/3 once the inertial subrange of turbulence scales is reached (e.g., Pope[45]). However, in the present case this regime is unlikely to have been reached by the current temporal capability. A rough estimate based on Kolmogorov scaling indicates the expected onset of the -5/3 slope would be above 20 kHz; adapting the simulations of Kawai and Lele[24] suggests about 30 kHz.

Nonetheless, a uniform slope appears to exist from about 5 – 25 kHz in spectra of the vertical velocity component shown in Fig. 12b. This slope appears consistent with a -1 dependency, which is well established at frequencies lower than those of the inertial subrange in pressure power spectra beneath wall-bounded turbulence (e.g., Bull[46]) but its existence in the velocity field remains elusive and controversial.[47,48] Nickels et al[49] provide an excellent summary of why it is so difficult to detect in wall-bounded turbulence. It is unclear from Fig. 12b whether the present dependency has been located because the jet-in-crossflow physics produce it at lower Reynolds numbers than in wall-bounded turbulence or whether the manifestation of PIV correlation noise and aliasing effects have coincidentally generated an apparent -1 slope.

An answer to this ambiguity may be found in still higher frequencies contained within the pulse-burst PIV data. In the 40 μs between successive velocity fields, the flow convects by about 16 vector spacings. The intervening 15 vectors all contain valid information that may be introduced to the temporal signals. If Taylor's Hypothesis may be assumed valid over this short distance and time, the local instantaneous convection velocity may be used to convert these additional vectors to smaller time steps to fill the temporal gaps between actual data acquisition intervals. Scarano and Moore[50] describe such a super-sampling algorithm and portray it as "pouring space into time." Fortunately, it is reasonable to employ Taylor's

Hypothesis on these brief scales, even for small scales of turbulence. Crucially, the super-sampling method employs local and instantaneous values for the convection velocity and direction rather than any averaged over time or space. Del Alamo and Jimenez[51] have shown this is necessary to yield an accurate representation of the turbulent energy spectra, which explains the success of Scarano and Moore's validation of the technique. An algorithm similar to Scarano and Moore's has been employed for the cross-correlated pulse-burst PIV; the auto-correlated data will yield inferior super-sampled information because the interrogation windows are larger and the correlations noisier, leading to poorer vector quality between time steps. The local instantaneous convection velocity was used to move forward in space along the local streamline from one time step and back in space from the subsequent time step, then these values were interpolated to produce intermediate vector fields. In addition, high-frequency noise was treated within the DaVis software package using a second-order polynomial fit over 3 × 3 vector windows; no other vector smoothing was used in this case.

The super-sampled power spectra are shown in Fig. 13. Since no significant difference between the upstream and downstream locations was noted, only a single location is used in Fig. 13, with the super-sampling acquired nearer to the center of the field of view where no edge effects interfere with following streamlines forward and backward to obtain convected vectors. The previous spectra from Fig. 12 are not shown superposed to allow a clear view of the new spectra, but they were found in good agreement with the super-sampled data until their noise floor rose.

The most consequential of the super-sampled spectra is the vertical component in Fig. 13b. The super-sampled results well match the auto-correlated data to the end of their range, then continue the -1 slope dependence to about 40 kHz before gradually transitioning to an apparent -5/3 slope dependence. The noise floor begins to show at about 150 kHz, even with the denoising algorithm that was employed. The presence of the -5/3 region, as remarked earlier, is well-known and expected as a consequence of the inertial subrange of turbulence decay. The -1 dependence, on the other hand, is an unanticipated discovery but appears to be substantiated by the super-sampled data. Note that the denoising algorithm and any remaining aliasing effects would influence frequencies well into the -5/3 regime and not those of the -1 regime (several denoising algorithms were tested and had a demonstrable influence only for frequencies exceeding about 100 kHz). The -1 regime lasts for a full decade, from approximately 4 – 40 kHz. The streamwise component in Fig. 13a appears to be supportive of a -1 slope dependence as well but its lack of a peak means this region does not initiate until about 8 kHz. The -5/3 slope dependence at high frequencies is somewhat less convincing for the streamwise component than for the vertical component.

The -1 regime occurs at frequencies lying between the inertial subrange and the spacing of large-scale vortices of common sign, the latter of which has been seen to be a distance of about 5 – 6 d_j. The inertial subrange appears to begin at about 40 kHz in Fig. 13b, which would correspond to a length scale of about 7 mm, or 0.7 d_j, at a convection velocity of

about 0.93-0.95 U_∞. Pope[45] suggests that the upper bound of the inertial subrange can be approximated as 1/6 of the integral length scale, whose value was calculated for the present conditions by Beresh et al[8] as 4.0 – 4.5 d_j. One-sixth of this is therefore 0.67 – 0.75 d_j, in remarkable agreement with the estimate derived from Fig. 13b. This scale is roughly comparable to the smallest visually discernable vortices in the PIV vector fields of Figs. 3 and 9. This would seem to indicate that vortices on the scale of 0.7 – 5 d_j are responsible for the behavior of the -1 regime, which would correspond to the dominant turbulent eddies observed by the present PIV measurements. Though this scaling law is physically plausible and consistent with estimates of turbulent length scales, the limited testing conditions of the present experiment must caution against drawing a generalized conclusion concerning compressible jets in crossflow.

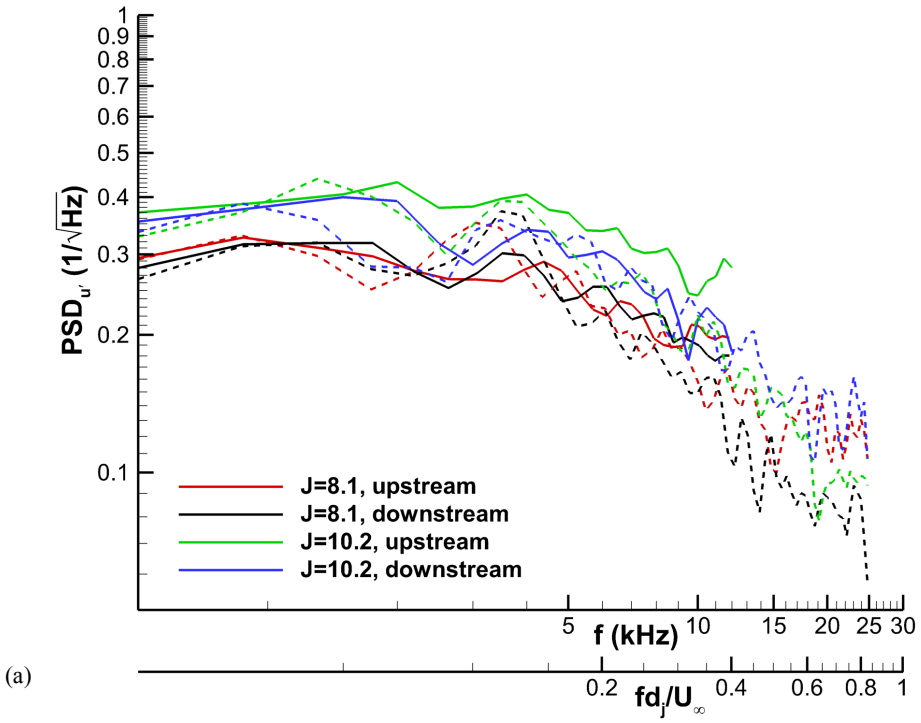

(a)

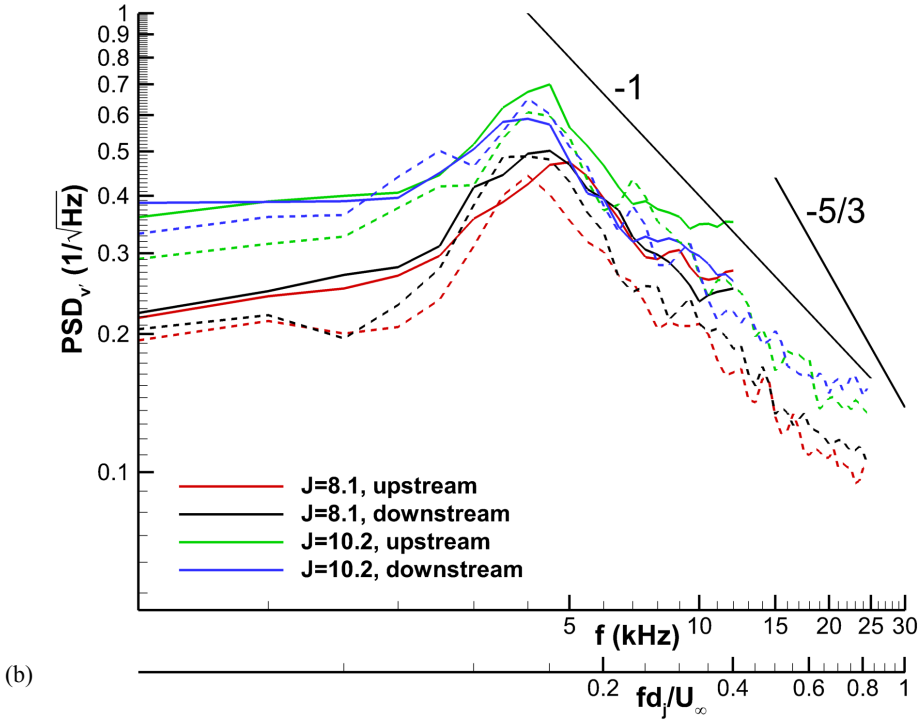

(b)

FIG. 12. Power spectra of velocity fluctuations at J=8.1 and J=10.2, measured at an upstream location in the field of view and a downstream location. Solid lines denote cross-correlation data at 25 kHz and broken lines are auto-correlation data at 50 kHz. (a) streamwise component; (b) vertical component.

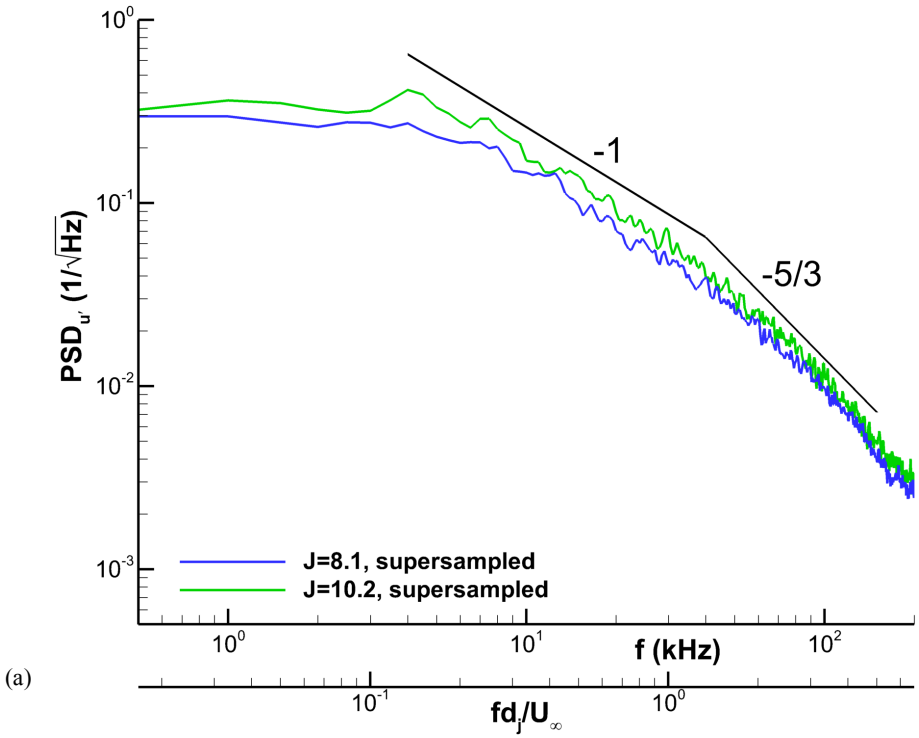

(a)

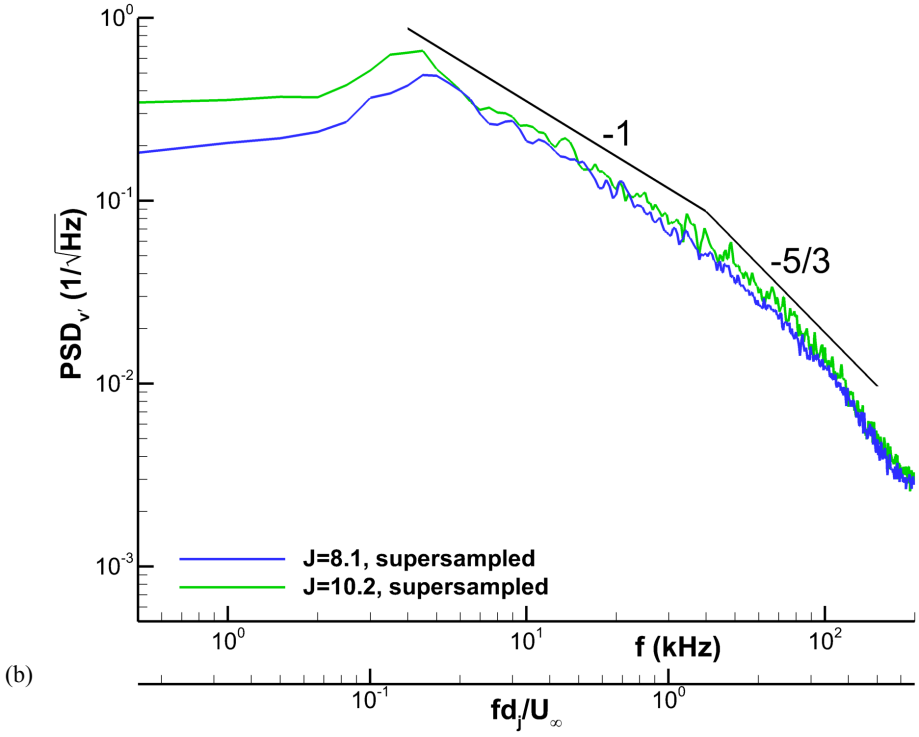

(b)

FIG. 13. Super-sampled power spectra of velocity fluctuations at J=8.1 and J=10.2, measured near the center of the field of view. (a) streamwise component; (b) vertical component.

CONCLUSIONS

Pulse-burst PIV has been employed to acquire time-resolved data at 25 kHz of a supersonic jet exhausting into a subsonic compressible crossflow. This variant of TR-PIV is necessary to obtain the temporal component of the velocity field in a high-speed ground testing facility. Data were acquired along the windward boundary of the jet shear layer with the freestream and can be used to identify the turbulent eddies as they convect downstream in the far-field of the interaction. Conditional ensemble averages, cross-correlations, and spectral analysis were used to analyze the measurements.

Turbulent eddies were found to have a tendency to occur in closely-spaced counter-rotating pairs, on the order of one jet diameter, and are routinely observed in the PIV movies. However, the variable orientation of these pairs plus the effects of interactions between different pairs of eddies makes them difficult to detect in a statistical sense. On a larger spacing, about three times the separation between pairs of eddies, the passage of correlated counter-rotating vortices are more strongly observed. As a turbulent eddy convects through the shear layer, correlated eddies of opposite sign commonly pass by at this spacing both leading and trailing the reference eddy. Taken together, these data indicate the paired nature of the turbulent eddies and the tendency for these pairs to recur at repeatable spacing. Velocity spectra reveal a peak at a frequency consistent with this recurring spacing between shear-layer vortices rotating with identical sign. The spatial scale of these vortices appears similar to previous observations of compressible jets in crossflow.

Finally, super-sampling the data to increase the bandwidth of the power spectra to about 150 kHz reveals two regions exhibiting slopes with a constant power-law dependence. One is the well-known inertial subrange with a slope of -5/3 at high frequencies. The other exhibits a -1 power-law dependence for a decade of mid-range frequencies lying between the inertial subrange and the frequency peak associated with the spacing of convecting eddy pairs. This corresponds to scales bounded by the integral length scale of the decaying jet plume and the smallest discernable vortices in the PIV movies, and thus the -1 power-law regime appears attributable to large-scale shear-layer eddies.

ACKNOWLEDGMENTS

The authors would like to acknowledge Sean Kearney and Daniel Guildenbecher of Sandia Labs and Naibo Jiang, Mikhail Slipchenko, Jason Mance, and Sukesh Roy of Spectral Energies for their assistance with experimental setup and data acquisition. In addition, the authors thank Srinivasan Arunajatesan, Matthew Barone and Edward DeMauro of Sandia Labs for helpful discussions interpreting the data and debating the physics of jets in crossflow.

This work is supported by Sandia National Laboratories and the United States Department of Energy. Sandia is a multiprogram laboratory managed and operated by Sandia Corporation, a wholly owned subsidiary of Lockheed Martin Corporation, for the United States Department of Energy's National Nuclear Security Administration under contract DE-AC04-94AL85000.

REFERENCES

[1] M. Wernet, "Temporally Resolved PIV for Space-Time Correlations in Both Cold and Hot Jet Flows," *Measurement Science and Technology*, **18**(5), 1387-1403 (2007).

[2] B. Brock, R. H. Haynes, B. S. Thurow, G. Lyons, and N. E. Murray, "An Examination of MHz Rate PIV in a Heated Supersonic Jet," AIAA Paper 2014-1102, 2014.

[3] J. D. Miller, J. B. Michael, M. N. Slipchenko, S. Roy, T. R. Meyer, and J. R. Gord, "Simultaneous High-Speed Planar Imaging of Mixture Fraction and Velocity using a Burst-Mode Laser," *Applied Physics B*, **113**, 93-97 (2013).

[4] J. D. Miller, J. R. Gord, T. R. Meyer, M. N. Slipchenko, J. G. Mance, and S. Roy, "Development of a Diode-Pumped, 100-ms Quasi-Continuous Burst-Mode Laser for High-Speed Combustion Diagnostics," AIAA Paper 2014-2524, 2014.

[5] S. J. Beresh, S. P. Kearney, J. L. Wagner, D. R. Guildenbecher, J. F. Henfling, R. W. Spillers, B. O. M. Pruett, N. Jiang, M. Slipchenko, J. Mance, and S. Roy, "Pulse-Burst PIV in a High-Speed Wind Tunnel," accepted for publication in *Measurement Science and Technology*, 2015.

[6] B. Thurow, N. Jiang, and W. Lempert, "Review of Ultra-High Repetition Rate Laser Diagnostics for Fluid Dynamic Measurements," *Measurement Science and Technology*, **24**(1), 012002 (2013).

[7] S. J. Beresh, J. F. Henfling, R. J. Erven, and R. W. Spillers, "Penetration of a Transverse Supersonic Jet into a Subsonic Compressible Crossflow," *AIAA Journal*, **43**(2), 379-389 (2005).

[8] S. J. Beresh, J. F. Henfling, R. J. Erven, and R. W. Spillers, "Turbulent Characteristics of a Transverse Supersonic Jet in a Subsonic Compressible Crossflow," *AIAA Journal*, **43**(11), 2385-2394 (2005).

[9] S. J. Beresh, J. F. Henfling, R. J. Erven, and R. W. Spillers, "Crossplane Velocimetry of a Transverse Supersonic Jet in a Transonic Crossflow," *AIAA Journal*, **44**(12), 3051-3061 (2006).

[10] A. R. Karagozian, "Transverse Jets and their Control," *Progress in Energy and Combustion Science*, **36**(5), 531-553 (2010).

[11] K. Mahesh, "The Interaction of Jets with Crossflow," *Annual Review of Fluid Mechanics*, **45**, 379-407 (2013).

[12] T. F. Fric and A. Roshko, "Vortical Structure in the Wake of a Transverse Jet," *Journal of Fluid Mechanics*, **279**, 1-47 (1994).

[13] R. M. Kelso, T. T. Lim, and A. E. Perry, "An Experimental Study of Round Jets in Cross-flow," *Journal of Fluid Mechanics*, **306**, 111-144 (1996).

[14] S. H. Smith and M. G. Mungal, "Mixing, Structure and Scaling of the Jet in Crossflow," *Journal of Fluid Mechanics*, **357**, 83-122 (1998).

[15] L. K. Su and M. G. Mungal, "Simultaneous Measurements of Scalar and Velocity Field Evolution in Turbulent Crossflowing Jets," *Journal of Fluid Mechanics*, **513**, 1-45 (2004).

[16] K. E. Meyer, J. M. Pedersen, and O. Ozcan, "A Turbulent Jet in Crossflow Analysed with Proper Orthogonal Decomposition," *Journal of Fluid Mechanics*, **583**, 199-227 (2007).

[17] S. Megerien, J. Davitian, L. S. de B. Alves, and A. R. Karagozian, "Transverse-Jet Shear-Layer Instabilities. Part 1. Experimental Studies," *Journal of Fluid Mechanics*, **593**, 93-129 (2007).

[18] D. R. Getsinger, L. Gevorkyan, O. I. Smith, and A. R. Karagozian, "Structural and Stability Characteristics of Jets in Crossflow," *Journal of Fluid Mechanics*, **760**, 342-367 (2014).

[19] L. S. de B. Alves, R. E. Kelly, and A. R. Karagozian, "Transverse-Jet Shear-Layer Instabilities. Part 2. Linear Analysis for Large Jet-to-Crossflow Velocity Ratio," *Journal of Fluid Mechanics*, **602**, 383-401 (2008).

[20] M. R. Gruber, A. S. Nejad, T. H. Chen, and J. C. Dutton, "Compressibility Effects in Supersonic Transverse Injection Flowfields," *Physics of Fluids*, **9**(5), 1448-1461 (1997).

[21] A. Ben-Yakar, M. G. Mungal, and R. K. Hanson, "Time Evolution and Mixing Characteristics of Hydrogen and Ethylene Transverse Jets in Supersonic Crossflows," *Physics of Fluids*, **18**(2), 026101 (2006).

[22] H. Takahashi, G. Masuya, and M. Hirota, "Effects of Injection and Main Flow Conditions on Supersonic Turbulent Mixing Structure," *AIAA Journal*, **48**(8), 1748-1756 (2010).

[23] J. C. Hermanson and M. Winter, "Mie Scattering Imaging of a Transverse, Sonic Jet in Supersonic Flow," *AIAA Journal*, **31**(1), 129-132 (1993).

[24] S. Kawai and S. K. Lele, "Large-Eddy Simulation of Jet Mixing in Supersonic Crossflows," *AIAA Journal*, **48**(9), 2063-2083 (2010).

[25] J. Watanabe, T. Kouchi, K. Takita, and G. Masuya, "Numerical Study on the Turbulent Structure of Transverse Jet into Supersonic Flow," *AIAA Journal*, **49**(9), 2057-2067 (2011).

[26] D. M. Peterson and G. V. Candler, "Simulations of Mixing for Normal and Low-Angled Injection into Supersonic Crossflow," *AIAA Journal*, **49**(12), 2792-2804 (2011).

[27] W. M. VanLerberghe, J. G. Santiago, J. C. Dutton, R. P. Lucht, "Mixing of a Sonic Transverse Jet Injected into a Supersonic Flow," *AIAA Journal*, **38**(3), 470-479 (2000).

[28] F. Genin and S. Menon, "Dynamics of Sonic Jet Injection into Supersonic Crossflow," *Journal of Turbulence*, **11**(4), 1-30 (2010).

[29] X. Chai and K. Mahesh, "Simulations of High Speed Turbulent Jets in Crossflows," AIAA Paper 2011-650, 2011.

[30] J. G. Santiago and J. C. Dutton, "Velocity Measurements of a Jet Injected into a Supersonic Crossflow," *Journal of Propulsion and Power*, **13**(2), 264-273 (1997).

[31] M. N. Slipchenko, J. D. Miller, S. Roy, J. R. Gord, S. A. Danczyk, and T. R. Meyer, "Quasi-Continuous Burst-Mode Laser for High-Speed Planar Imaging," *Optics Letters*, **37**(8), 1346-1348 (2012).

[32] M. N. Slipchenko, J. D. Miller, S. Roy, J. R. Gord, and T. R. Meyer, "All-Diode-Pumped Quasi-Continuous Burst-Mode Laser for Extended High-Speed Planar Imaging," *Optics Express*, **21**(1), 681-689 (2013).

[33] M. N. Slipchenko, J. D. Miller, S. Roy, T. R. Meyer, J. G. Mance, and J. R. Gord, "100-kHz, 100-ms, 400-J Burst-Mode Laser with Dual-Wavelength Diode Amplifiers," *Optics Letters*, **39**(16), 4735-4738 (2014).

[34] Z. M. Moussa, J. W. Trischka, and S. Eskinazi, "The Near Field in the Mixing of a Round Jet with a Cross-Stream," *Journal of Fluid Mechanics*, **80**(1), 49-80 (1977).
[35] J. Andreopoulos, "On the Structure of Jets in a Crossflow," *Journal of Fluid Mechanics*, **157**, 163-197 (1985).
[36] J. Watanabe, T. Kouchi, K. Takita, and G. Masuya, "Large-Eddy Simulation of Jet in Supersonic Crossflow with Different Injectant Species," *AIAA Journal*, **50**(12), 2765-2778 (2012).
[37] J. N. Blanchard, Y. Brunet, and A. Merlen, "Influence of a Counter Rotating Vortex Pair on the Stability of a Jet in a Cross Flow: An Experimental Study by Flow Visualizations," *Experiments in Fluids*, **26**(1-2), 63-74 (1999).
[38] R. Camussi, G. Guj, and A. Stella, "Experimental Study of a Jet in a Crossflow at Very Low Reynolds Number," *Journal of Fluid Mechanics*, **454**, 113-144 (2002).
[39] S. Bagheri, P. Schlatter, P. J. Schmid, and D. S. Henningson, "Global Stability of a Jet in Crossflow," *Journal of Fluid Mechanics*, **624**, 33-44 (2009).
[40] P. Schlatter, S. Bagheri, and D. S. Henningson, "Self-Sustained Global Oscillations in a Jet in Crossflow," *Theoretical and Computational Fluid Dynamics*, **25**, 129-146 (2011).
[41] D. R. Getsinger, C. Hendrickson, and A. R. Karagozian, "Shear Layer Instabilities in Low-Density Transverse Jets," *Experiments in Fluids*, **53**(3), 783-801 (2012).
[42] R. M. Kelso, T. T. Lim, and A. E. Perry, "An Experimental Study of Round Jets in Cross-Flow," *Journal of Fluid Mechanics*, **306**, 111-144 (1996).
[43] T. Cambonie and J.-L. Aider, "Transition Scenario of the Round Jet in Crossflow Topology at Low Velocity Ratios," *Physics of Fluid*s, **26**(8), 084101 (2014).
[44] T. H. New, T. T. Lim, and S. C. Luo, "Effects of Jet Velocity Profiles on a Round Jet in Cross-Flow," *Experiments in Fluids*, **40**(6), 859-875 (2006).
[45] S. B. Pope, *Turbulent Flows* (Cambridge University Press, 2000), pp. 228-242.
[46] M. K. Bull, "Wall-Pressure Fluctuations Beneath Turbulent Boundary Layers: Some Reflections on Forty Years of Research," *Journal of Sound and Vibration*, **190**(3), 299-315 (1996).
[47] A. E. Perry, S. Henbest, and M. S. Chong, "A Theoretical and Experimental Study of Wall Turbulence," *Journal of Fluid Mechanics*, **165**, 163-199 (1986).
[48] T. B. Nickels, I. Marusic, S. Hafez, and M. S. Chong, "Evidence of the k_1^{-1} Law in a High-Reynolds-Number Turbulent Boundary Layer," *Physical Review Letters*, **95**(7), 074501 (2005).
[49] T. B. Nickels, I. Marusic, S. Hafez, N. Hutchins, and M. S. Chong, "Some Predictions of the Attached Eddy Model for a High Reynolds Number Boundary Layer," *Philosophical Transactions of the Royal Society A*, **365**(1852), 807-822 (2007).
[50] F. Scarano and P. Moore, "An Advection-Based Model to Increase the Temporal Resolution of PIV Time Series," *Experiments in Fluids* **52**(4), 919-933, 2012.
[51] J. C. Del Alamo and J. Jimenez, "Estimation of Turbulent Convection Velocities and Corrections to Taylor's Approximation," *Journal of Fluid Mechanics*, **640**, 5-26 (2009).